ASM Handbook, Volume 1A, *Cast Iron Science and Technology*
D.M. Stefanescu, editor

The Liquid State and Principles of Solidification of Cast Iron

Doru M. Stefanescu, The Ohio State University and The University of Alabama
Roxana Ruxanda, Emerson Climate Technologies

UPON MELTING OF GRAPHITIC IRON, the graphite will dissolve if enough time at the superheating temperature is allowed. Thus, the structure of liquid iron is a function of chemical analysis, temperature, and holding time in the liquid state. X-ray analysis on liquid cast iron demonstrated that, for a Fe-4.1%C-1%Si alloy, the size of undissolved graphite immediately after melting was 36 to 38 nm (Ref 1). It decreased by half after 5 to 6 h holding at 1220 °C (2230 °F). The graphite completely dissolved after approximately 11 h. For a low-silicon alloy, Fe-4% C-0.02%Si, the size of the graphite particles after melting was approximately 17 nm, and the graphite dissolved completely in 3 to 5 h.

Iron-carbon alloys with low carbon content (steels) in liquid state are condensed phases with compact distribution of atoms in short-range order. X-ray and neutron wide-angle diffraction performed by Steeb and Maier (Ref 2) on molten iron-carbon alloys with up to 5.5 wt% C in the temperature range of 1150 to 1600 °C (2100 to 2910 °F) found that, for pure iron, the number of nearest neighbors (number of atoms in the first coordination sphere) is $N^I = 9$, and the nearest neighbor distance is $r^I = 2.6 \cdot 10^{-10}$ m. Up to 1% C, the packing density is increased as the distance increases to $2.67 \cdot 10^{-10}$ m, and the number of neighbors increases to 10.4 (Fig. 1). Between 1.8 and 3% C, the nearest neighbor distance remains constant, but the number of neighbors increases to 11.2 atoms, which means that the packing density is further increased. A maximum packing density is reached at 3% C, and it remains constant at higher carbon concentrations. At 3.5% C, the authors concluded that short-range-ordered regions rich in carbon exist in the melt, but they were unable to establish their structure. Indeed, viscosity measurements summarized in Fig. 2 (Ref 3) show a correlation between viscosity and percentage of carbon. The melts containing short-range-ordered regions show high viscosity values.

Thus, liquid iron-carbon alloys with low carbon content (<3.5% C, i.e., steels and cast irons poor in carbon) are microscopically homogeneous. Liquid iron-carbon alloys with high carbon (>3.5% C, i.e., cast irons rich in carbon) are colloidal-dispersed systems with carbon clusters in liquid solution. The nature of the carbon clusters is not clear. There are two hypotheses regarding their structure: they are Fe_3C molecules, or they are C_n molecules.

From thermodynamic considerations, Darken (Ref 4) concluded that the existence of Fe_3C molecules in iron-carbon melts is possible. Activity measurements also support short-range order similar to Fe_3C (Ref 5). Because the nucleation energy for Fe_3C is smaller than that for graphite, it is thermodynamically possible for the carbon-rich regions to exist as Fe_3C clusters.

Other investigators consider the carbon clusters to be stable in iron-carbon melts with more than 2% C (Ref 6, 7). Their size is supposed to be in the range of 1 to 20 nm, and it increases with the carbon equivalent, lower silicon content, and lower holding time and temperature. According to Ref 2, these carbon clusters contain approximately 15 atoms (C_{15}) with a stability time interval of approximately 10^{-10} s. It is to be expected that the carbon-rich clusters existing in molten iron-carbon alloys are in dynamic equilibrium and that they diffuse within the melt.

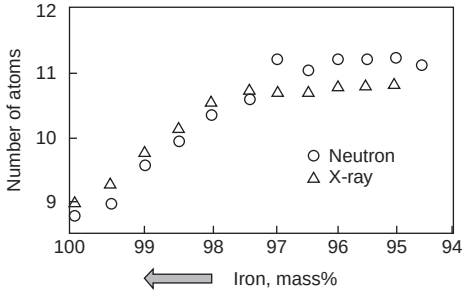

Fig. 1 Number of atoms in the first coordination sphere obtained by neutron diffraction and x-ray. Source: Ref 2

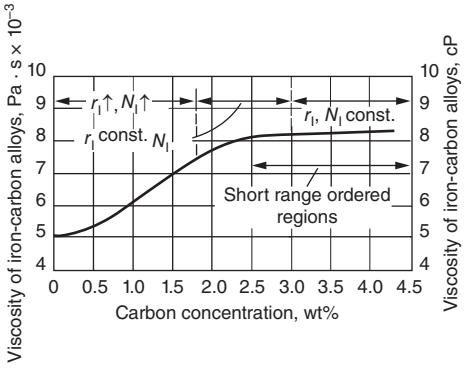

Fig. 2 Viscosity of iron-carbon alloys as a function of carbon concentration. Source: Ref 3

Fundamentals of Solidification of Cast Iron

Solidification processing is one of the oldest manufacturing processes, because it is the principal component of metal casting processing. While solidification science evolved from the need to better understand and further develop casting processes, solidification science today (2106) is at the base of many new developments that fall out of the realm of traditional metal casting.

Solidification is, strictly speaking, the transformation of liquid matter into solid matter. The microstructure that results from solidification may be the final one, in which case it directly affects the mechanical properties of the product. In other cases, heat treatment or other processes may be used after solidification to further modify the solidification microstructure. However, the outcome of this additional processing will be greatly affected by the solidification microstructure.

Length Scale of Solidification Structures

The effect of solidification on the morphology of the matrix can be deconstructed at four different length scales (Ref 8) (Fig. 3):

- *The macroscale (macrostructure)* is of the order of 10^{-3} to 1 m. Elements of the macroscale include shrinkage cavity, macrosegregation, cracks, surface roughness (finish), and casting dimensions. A typical example of a solidification macrostructure is given in Fig. 4, after Boeri and Sikora (Ref 9), which illustrates columnar grains growing inward into the cast iron rod.
- *The mesoscale* is of the order of 10^{-4} m. It allows description of the microstructure features at the grain level, without resolving the intricacies of the grain structure. As seen in Fig. 3, the solid/liquid (S/L) interface is not sharp. Three regions can be observed: liquid, mushy (containing both liquid and solid grains), and solid. Mechanical properties are affected by the solidification structure at the mesoscale level, which is described by features such as grain size and type (columnar or equiaxed), the type and concentration of chemical microsegregation, and the amount of microshrinkage, porosity, and inclusions. The term *mesoscale* has been introduced in solidification science to more accurately describe the results of computer models. An example of a solidification mesoscale structure is given in Fig. 5, after Moore (Ref 10).
- *The microscale (microstructure)* is of the order of 10^{-6} to 10^{-5} m. The microscale describes the complex morphology of the solidification grain. In a sound casting, mechanical properties depend on the solidification structure at the microscale level. To evaluate the influence of solidification on the properties of the castings, it is necessary to know the as-cast grain morphology (i.e., size and type, columnar or equiaxed) and the length scale of the microstructure (interphase spacing, e.g., dendrite arm spacing and eutectic lamellar spacing). The term *microstructure* is the classic term used in metallography to describe features observed under the microscope, as seen in the micrograph from Fig. 6, which shows graphite and pearlite in a gray iron.
- *The nanoscale (atomic scale)* is of the order of 10^{-9} m (nanometers) and describes the atomic morphology of the S/L interface. At this scale, nucleation and growth kinetics of solidification are discussed in terms of the transfer of individual atoms from the liquid to the solid state. Features such as dislocations, atomic layers, and even individual atoms are observed with electronic microscopes. An example of graphite layers in a spheroidal graphite aggregate seen at nanoscale magnification is given in Fig. 7, after Purdy and Audier (Ref 11).

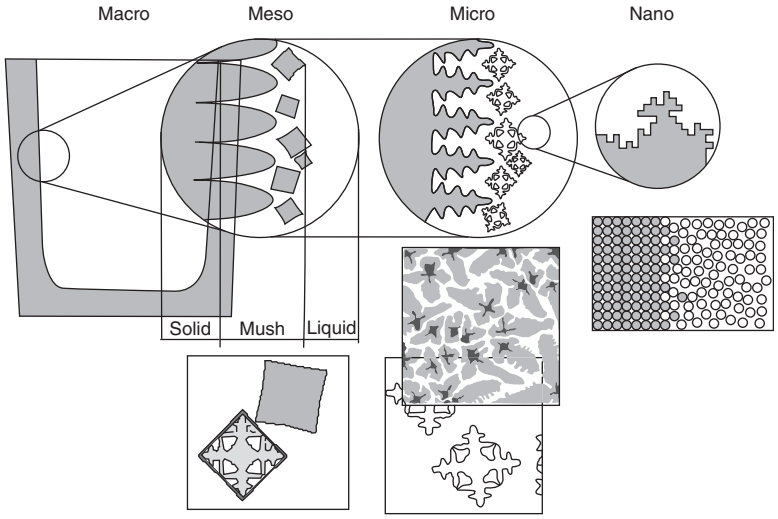

Fig. 3 Solidification length scale. Source: Ref 8

As discussed in some detail in the following sections, two basic phenomena must take place in the liquid for solidification to occur: undercooling and nucleation. If these conditions are met, the nuclei can grow into the new solid grains.

Undercooling

Global equilibrium phase diagrams are frequently used to understand alloy behavior when the alloy is cooled from the liquid state to room temperature. Global equilibrium requires uniform chemical potentials and temperature across the system. Under such conditions, no changes occur with time. When global equilibrium exists, the fraction of phases can be calculated with the lever rule, and the phase diagram gives the uniform composition of the liquid and solid phases. Such conditions exist only when the solidification velocity is much smaller than the diffusion velocity. Uniform chemical potentials and temperature may truly appear only when solidification takes place over geological times.

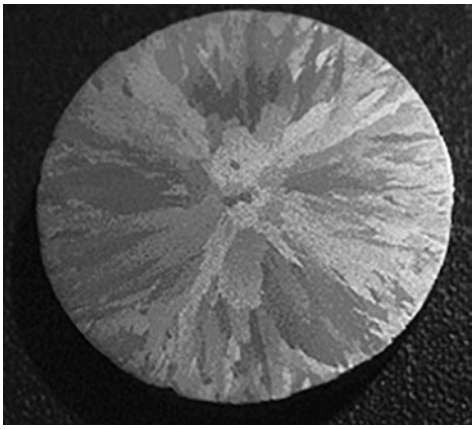

Fig. 4 Macrostructure of 30 mm (1.2 in.) diameter bars showing columnar grains (primary austenite dendrites). Source: Ref 9

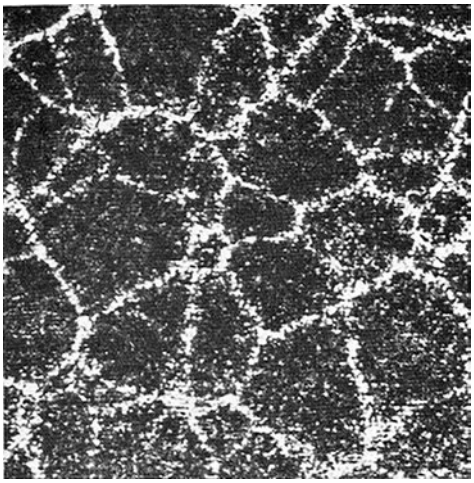

Fig. 5 Room-temperature eutectic grain structure in lamellar graphite iron. Original magnification: 14×. Source: Ref 10

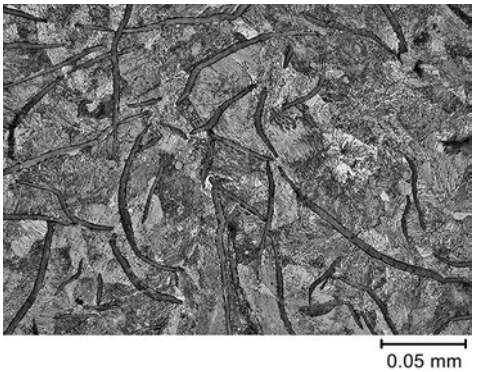

Fig. 6 Pearlitic gray iron showing type A graphite and fine pearlite

Solidification as encountered in common processes does not occur at equilibrium, because during solidification of most castings, both temperature and composition gradients exist across the casting. Elementary thermodynamics demonstrates that a liquid cannot solidify unless some undercooling below the equilibrium (melting) temperature, T_e, occurs. Five types of solidification undercooling have been identified: kinetic undercooling, thermal undercooling, constitutional (solutal) undercooling, curvature undercooling, and pressure undercooling.

Nevertheless, in most cases, the overall solidification kinetics can be described with sufficient accuracy by using the local equilibrium condition, that is, by using the mass, energy, and species transport equations to express the temperature and composition variation within each phase and by using equilibrium phase diagrams to evaluate the temperature and composition of phase boundaries, such as the S/L interface (corrections must be made for interface curvature). Most phase transformations, with the exception of massive (partitionless) and martensitic transformations, can be described with the local equilibrium condition. When the stable phase cannot nucleate or grow sufficiently fast (e.g., gray-to-white transition in cast iron), metastable local equilibrium can occur. For both stable and metastable local equilibria, the chemical potentials of the components across the interface must be equal for the liquid and for the solid.

However, at large undercooling, the solidification velocity exceeds the diffusive speed of solute atoms in the liquid phase (rapid solidification). The solute is trapped into the solid at levels exceeding the equilibrium solubility. Typically, for solute trapping, the solidification velocity must exceed 5 m/s (16 ft/s).

Kinetic Undercooling. When a number of simplifying assumptions are introduced (pure metal, constant pressure, no thermal gradient in the liquid, and flat S/L interface—that is, the radius of curvature of the interface is $r = \infty$), the only undercooling driving the S/L interface is the kinetic undercooling. It is a nanoscale length effect, resulting from the net difference in atoms transported from L to S and from S to L. Typically for metals, the kinetic undercooling is very small, of the order of 0.01 to 0.05 K.

When the simplifying assumptions are relaxed to reflect typical solidification scenarios, the free energy of the liquid-solid system upon the solidification of a discrete volume of liquid, ΔF_v, will increase by:

$$\Delta F_v = \Delta G_T + \Delta G_c + \Delta G_r + \Delta F_P \quad \text{(Eq 1)}$$

where F and G are the Helmholtz and Gibbs free energy, respectively. The four right-hand terms are the change in free energy because of temperature, composition, curvature, and pressure variation, respectively. Solidification cannot occur unless each of these energies is balanced by a corresponding undercooling of the system, as discussed in this section.

Thermal Undercooling. If nucleation does not occur, a pure metal can undercool under the equilibrium temperature because of heat extraction. The liquid is said to be thermally undercooled by a quantity:

$$\Delta T_T = T_e - T^* \quad \text{(Eq 2)}$$

where ΔT_T is the thermal undercooling, T_e is the equilibrium (melting) temperature of the interface, and T^* is the S/L interface temperature.

Constitutional (Solutal) Undercooling. During alloy solidification, solute is rejected by the solid. This can be understood from the phase diagram in Fig. 8. For a given temperature, T^*, the composition of the solid, C_S, is smaller than that of the liquid, C_L, in equilibrium with the solid. The ratio $k = C_S/C_L$ is called the partition coefficient. For the case in the figure (where the equilibrium temperatures decrease with increased alloy composition), $k < 1$. The slope of the liquidus line is $m_L = dT_L/dC_L$, where T_L is the liquidus temperature.

Because of solute rejection, a boundary layer, richer in solute than the bulk liquid, is formed at the S/L interface. A direct consequence of this phenomenon is that the liquidus temperature is lower next to the interface than away from it (Fig. 9). The heat flow from the liquid to the solid imposes a thermal gradient, G_T, which dictates the local temperature in the melt. If the thermal gradient is lower than the liquidus gradient, G_L (the tangent to T_L at the S/L interface), which is the case shown in Fig. 9, the temperature in the boundary layer will be lower than the equilibrium liquidus temperature. Thus, a constitutionally undercooled region will result. The magnitude of the local constitutional (solutal) undercooling can be calculated as a function of the local composition as:

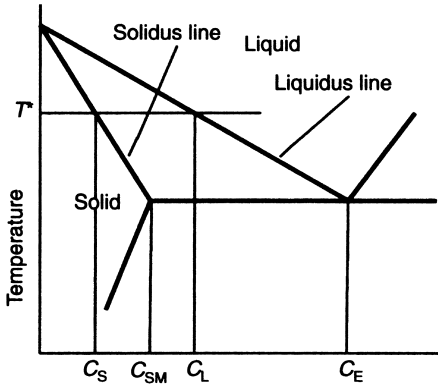

Fig. 8 Left corner of a phase diagram. T^*, interface temperature; T_S, solidus temperature; T_L, liquidus temperature; C_S, composition of the solid; C_{SM}, maximum solubility in the solid; C_L, composition of the liquid; C_E, eutectic composition

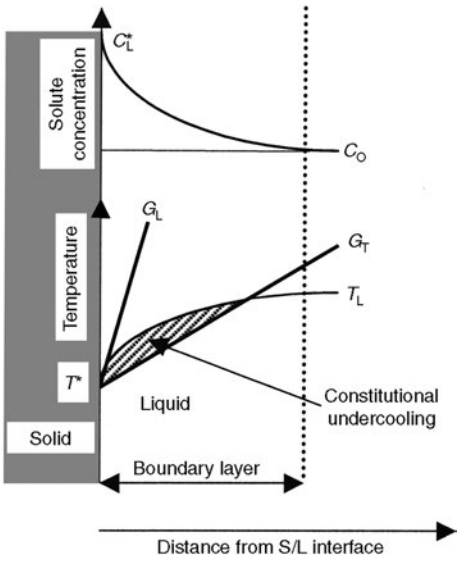

Fig. 9 Formation of a constitutionally undercooled region (dashed area) in the liquid next to the solid/liquid (S/L) interface because of the lower liquidus temperature produced by the higher solute content. C_L^*, composition of the liquid; C_o, bulk composition of the alloy at the beginning of solidification; G_L, liquidus (solutal) temperature gradient; G_T, thermal gradient in the liquid; T_L, liquidus temperature

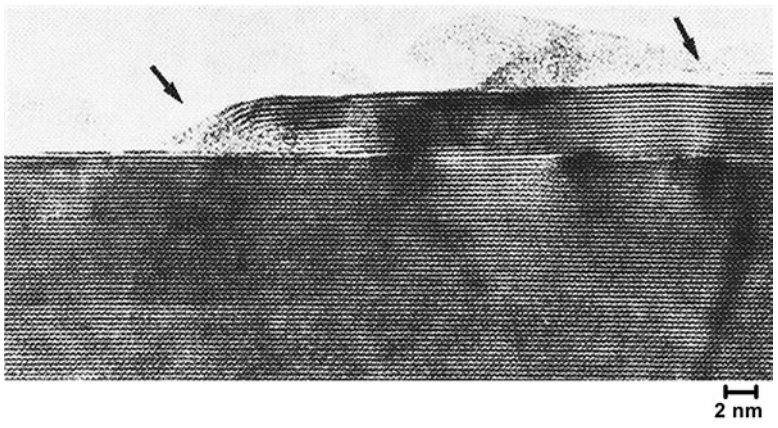

Fig. 7 Transmission electron microscopy image of a fractured graphite spheroid showing crystallization sites (indicated by arrows) of amorphous graphite. Source: Ref 11

$$\Delta T_c = T_L - T^* = -m\,(C_L^* - C_o) \quad \text{(Eq 3)}$$

where ΔT_c is the constitutional undercooling, C_L^* is the composition of the liquid, C_o is the bulk composition of the alloy at the beginning of solidification, and the other terms are as previously defined.

Curvature Undercooling. When a discrete liquid volume becomes solid, the newly formed S/L interface produces an increase in the energy of the system through the interface energy associated with it. For solidification to continue, additional undercooling is required. This undercooling is called the curvature undercooling. Because a smaller radius (higher curvature) of the solid results in a higher surface-to-volume ratio, higher curvature is associated with higher undercooling; thus:

$$\Delta T_r = T_e - T_e^r = \frac{\gamma}{\Delta S_f} K = \Gamma K \quad \text{(Eq 4)}$$

where ΔT_r is the curvature undercooling, T_e^r is the equilibrium temperature for a sphere of radius r, γ is the S/L interface energy, ΔS_f is the entropy of fusion, $K = 1/r$ is the curvature, and Γ is the Gibbs-Thomson coefficient.

Pressure Undercooling. An increase in the pressure applied to the liquid, ΔP, will cause an increased undercooling of the liquid, called pressure undercooling, ΔT_P. It can be calculated as:

$$\Delta T_P = \Delta P \cdot \Delta v / \Delta S_f \quad \text{(Eq 5)}$$

where Δv is the change in volume. For metals, the pressure undercooling is rather small, of the order of 10^{-2} K/atm. Therefore, typical pressure changes for usual processes have little influence on the melting temperature, and the pressure undercooling is negligible.

Undercooling is a basic condition required for solidification. However, for solidification to occur, nuclei must form in the liquid.

Nucleation

It is convenient to classify the types of nuclei available in the melt as resulting from homogeneous nucleation, heterogeneous nucleation, and dynamic nucleation (Ref 8).

Homogeneous Nucleation. When growth is initiated on substrates having the same chemistry as the solid, it is said that homogeneous nucleation has occurred. It is not common in casting alloys. However, it was demonstrated that, under certain conditions, graphite can nucleate on carbon-rich regions in the liquid iron that can be considered homogeneous nuclei (Ref 12).

Heterogeneous nucleation is based on the assumption that the development of the grain structure occurs upon a family of substrates of different chemistry than that of the solid. Heterogeneous nucleation occurs when substrate particles are deliberately introduced into a melt to promote equiaxed grain formation. This is common practice in liquid processing of cast iron because they are inoculated with specially designed alloys.

Heterogeneous nucleation is influenced by the solid metal/solid nucleus interface energy. The value of this energy depends on the crystal structure of the two phases. The interface between two crystals can be coherent, semicoherent, or incoherent.

Coherent interfaces may have slight deviations in the interatomic spacing, which causes lattice deformation and induces a strain in the lattice (Fig. 10). If the deviation in spacing is too large to be accommodated by strain, dislocations may form in distorted areas. The interface is said to be semicoherent. If there is no crystallographic matching between the two lattices, the structure changes abruptly from one crystal to the other; the interface is incoherent.

An efficient heterogeneous nucleant (inoculant) should satisfy the following requirements:

- The substrate must be solid in the melt; its melting point must be higher than the melt temperature, and it must not dissolve in the melt.
- There must be a low contact angle between the metal and nucleant particles or a high surface energy between the liquid and the nucleant.
- The nucleant must expose a large area to the liquid; this can be achieved by producing a fine dispersion of nucleant or by using a nucleant with a rough surface geometry.
- Because the atoms are attaching to the solid lattice of the substrate, the closer the substrate lattice resembles that of the solid phase, the easier nucleation will be. This means that, ideally, the crystal structure of the substrate and the solid phase should be the same, and that their lattice parameters should be similar (isomorphism). They should have at least analogous crystalline planes (epitaxy). Because the crystal structures of the solidifying alloy and the substrate may be different, the substrate must have one or more planes with atomic spacing and distribution close to that of one of the planes of the solid to be nucleated (coherent or semicoherent interface), that is, have a low linear disregistry, δ (Ref 13):

$$\delta = (a_n - a_S)/a_S \quad \text{(Eq 6)}$$

where a_n and a_S are the interatomic spacing along shared low-index crystal directions in the nucleant and the solid nucleus, respectively.

- Low symmetry lattice (complex lattice) is desirable. While it is impossible to assign numbers to lattice symmetry, to some extent the entropy of fusion can be used as a measure of lattice symmetry. In general, less symmetrical lattices have higher entropies of fusion.
- It should have the ability to nucleate at very low undercooling.

Inoculation and Grain Refining. The nucleation concepts introduced in the preceding paragraphs are helpful in the understanding of the widely used inoculation processes of cast iron. Inoculation is often used in cast iron processing to control the grain and graphite size and, to a lesser extent, graphite morphology. Typical inoculants for cast iron are based on ferrosilicon or calcium silicide. Inoculation must not be confused with modification. Modification, typically obtained through magnesium additions to the melt, is a process related mostly to graphite growth and morphology. The main purpose of inoculation is to promote grain refinement and avoid metastable solidification (chill), while modification is used to change the morphology of the eutectic aggregates.

Bramfitt (Ref 14) argued that the Turnbull/Vonnegut equation for linear disregistry (Eq 6) cannot be applied to crystallographic combinations of two phases with planes of differing atomic arrangements (e.g., cubic iron and hexagonal tungsten carbide). He modified the equation in terms of angular difference between the crystallographic directions within the plane to produce the planar disregistry equation:

$$\delta_{(hkl)_n}^{(hkl)_S} = \sum_{i=1}^{3} \frac{\left| \left(d_{[uvw]_S^i} \cos\theta \right) - d_{[uvw]_n^i} \right|}{d_{[uvw]_n^i}} \Big/ 3 \times 100 \quad \text{(Eq 7)}$$

where $(hkl)_S$ is a low-index plane of the substrate, $[uvw]_S$ is a low-index direction in $(hkl)_S$, $(hkl)_n$ is a low-index plane in the nucleated solid,

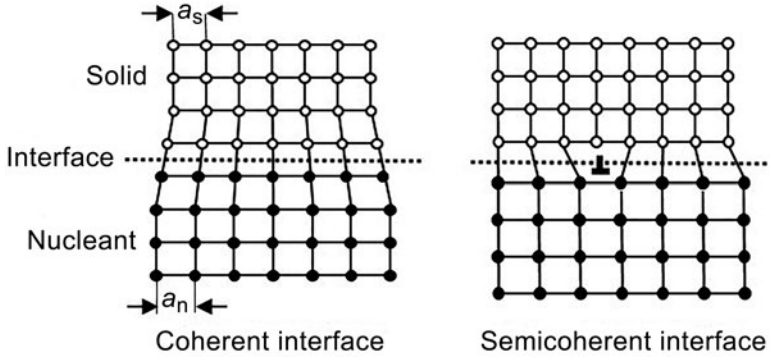

Fig. 10 Coherent and semicoherent interfaces. Source: Ref 8

$[uvw]_n$ is a low-index direction in $(hkl)_n$, is the interatomic spacing along $[uvw]_n$, $d_{[uvw]_S}$ is the interatomic spacing along $[uvw]_S$, and θ is the angle between $[uvw]_S$ and $[uvw]_n$. The effect of selected carbide and nitride additions to pure iron (99.95%) were then evaluated. Their effectiveness as nucleants was estimated based on the effect of the solidification undercooling. A good nucleant produced a lower undercooling. The main results are listed in Table 1 together with the planar disregistry between the nucleant and iron. It is observed that the highly effective inoculants have low disregistry (<12). It must be noted that, for cubic metals, there was no difference between the linear and planar disregistry. There is a parabolic relationship between the critical undercooling for nucleation and the disregistry: $\Delta T_{cr} = 0.25\ \delta^2$.

The size distribution of the nucleant is critical for heterogeneous nucleation. According to the free-growth theory developed by Greer et al. (Ref 15), the larger particles are more potent for heterogeneous nucleation and become active first. Only a small fraction of the particles become active before the onset of recalescence. A narrow size distribution of particles is more efficient for heterogeneous nucleation.

Another critical parameter for heterogeneous nucleation is the wettability of the nucleant. The wetting problem can be solved practically by the formation of an intermediate phase that wets the nucleant. Multistep nucleation mechanisms have been proposed for lamellar and spheroidal graphite cast irons, as summarized in Ref 8. Typical compositions of inoculants for cast iron are summarized in Table 2, after Elliott (Ref 16).

Dynamic nucleation occurs because of the action of convective currents within the melt. The initial chilling action of the mold may induce local solid grain formation. These grains are then carried into the bulk by fluid flow and survive and grow in the undercooled liquid. This is called the "big bang" mechanism.

Another possible mechanism for dynamic nucleation is the fragmentation of existing crystals through ripening and local remelting of columnar dendrites. The detached dendrite arms are carried to the center of the mold by convection currents, as shown in Fig. 11, after Trivedi and Kurz (Ref 17). If the center of the mold is undercooled, these crystals act as nuclei for equiaxed grains.

The number of grains identified by metallographic techniques at the end of solidification is not necessarily equal to the number of initial nuclei. Some nuclei may redissolve because of insufficient undercooling, while others may grow and coalesce, thus decreasing the final number of grains. As demonstrated through liquid quenching experiments on gray cast iron (Ref 18, 19), the final eutectic volumetric grain density was found to be as much as 27% less than the maximum number of grains developed during solidification (Fig. 12).

Growth and Interface Stability

The thermal and compositional fields at the S/L interface determine the morphology of the interface. During growth, local perturbations (instabilities) will form at the S/L interface. If the perturbations cannot survive, the interface remains planar (Fig. 13a). If, on the contrary, they become stable, they will continue to develop, and different interface morphologies can result (Fig. 13b–d). In pure metals, the only source of growing interface instabilities is the thermal field (thermal undercooling). In alloys, both thermal and solutal instabilities may grow, as a result of thermal and solutal undercooling.

When the thermal gradient in the liquid at the S/L interface is less than the liquidus temperature gradient, that is, $G_T < G_L$ (Fig. 9), the liquid at the interface (T^*) is at a lower temperature than its liquidus (T_L). This liquid is constitutionally undercooled. Instabilities growing in this region will become stable, because they will find themselves at a temperature lower than their equilibrium temperature. They will continue to grow. On the contrary, if $G_T > G_L$, the interface will remain planar (Fig. 13a).

For small constitutional undercooling, the instabilities will only grow in the solidification direction (the x-direction), and a cellular interface will result (Fig. 13b, c). This is shown in Fig. 14. The planar-to-cellular transition occurs at a gradient $G_{p/c}$. As the constitutional undercooling increases because of the lower thermal gradient, the spacing between the cells increases, and constitutional undercooling may also occur perpendicular to the growth direction (in the y-direction). Instabilities will develop on the sides of the cells, resulting in the formation of dendrites (Fig. 13d). This is the cellular-to-dendrite transition. It takes place at a temperature gradient $G_{c/d}$. Both cellular and dendritic growth occurring from the wall in the direction opposite to the heat transport can be described as columnar growth.

If constitutional undercooling is greater, equiaxed grains can be nucleated in the liquid away from the interface. The dendritic-to-equiaxed transition occurs at $G_{d/e}$. If the thermal gradient is almost flat, that is, $G_T = 0$, the driving force for the columnar front will be extremely small. A complete equiaxed structure is expected.

Table 1 Nucleating compounds for pure iron

Nucleant	Crystal structure	Undercooling, °C	Undercooling, °F	Disregistry relative to ferrite, %	Effectiveness
None	Cubic	30–55	85–130	···	···
TiN	Cubic	1.7	35.1	3.9	High
TiC	Cubic	1.8	35.2	5.9	High
ZrN	Cubic	7.0	45	11.2	Moderate
ZrC	Cubic	13.6	56.5	14.4	Low
WC	Hexagonal	16.1	61.0	12.7	Low

Table 2 Typical compositions of inoculants

Inoculant	Composition, mass%							
	Si	Al	Ca	Ba	Sr	Zr	Mn	Others
Standard FeSi	75–80	1.2–2	0.3–1.2	···	···	···	···	···
FeSi-Mn-Zr	60–65	1.2	1–3	···	···	5.6	5.6	···
FeSi-Ba	60–65	0.5–1.7	1.0	9–11	···	···	···	···
FeSi-Ba	60–65	1.5	2.0	5–6	···	···	9–10	···
FeSi-Zr	80	1.5–2.5	2.5	···	···	1.5	···	···
FeSi-Sr	75	<0.5	<0.1	···	0.8	···	···	···
FeSi-Ti	45–50	1.5	6	···	···	···	···	10 Ti
FeSi-Ce	45	0.5	0.5	···	···	···	···	13 RE
CaSi	60	1–2	30	···	···	···	···	···
FeSi-La	75	1.5	···	···	···	···	···	2 La
Graphite	···	···	···	···	···	···	···	99 C
FeSi + graphite	40–50	1.0	1.5	···	···	···	···	45

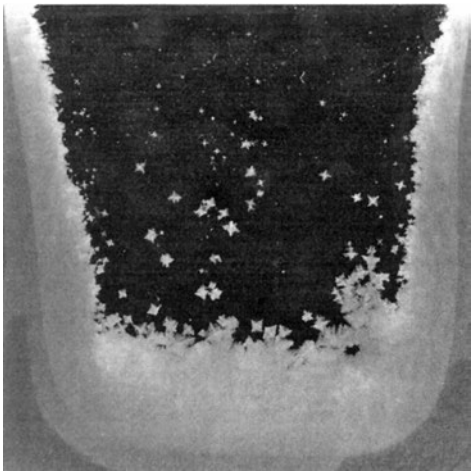

Fig. 11 Broken dendrite branches transported in the center of the ingot by liquid convection in an ammonium chloride/water system. Source: Ref 17

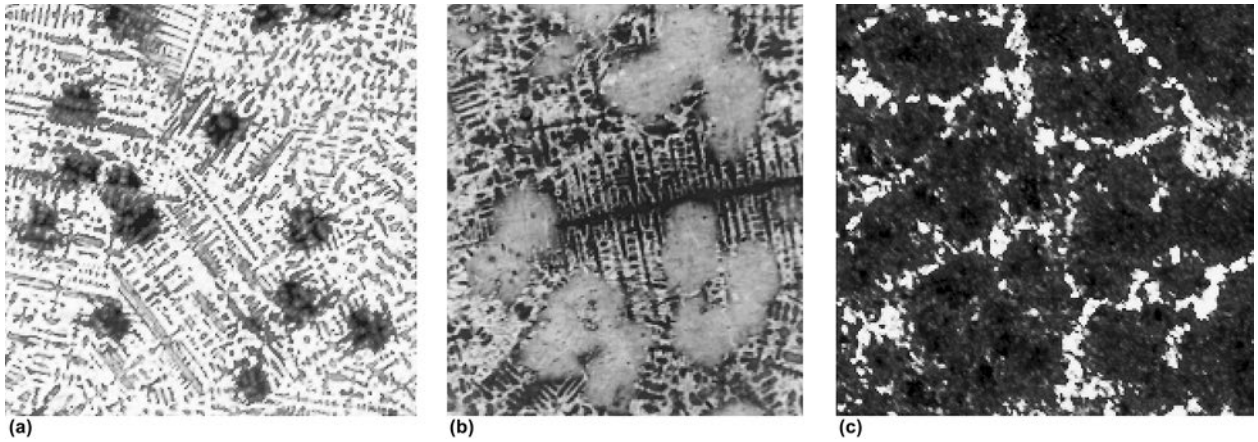

Fig. 12 Nucleation and coalescence of eutectic grains in cast iron. (a) Early solidification. (b) Late solidification. (c) After solidification (room temperature). Original magnification: 20×. Source: Ref 18

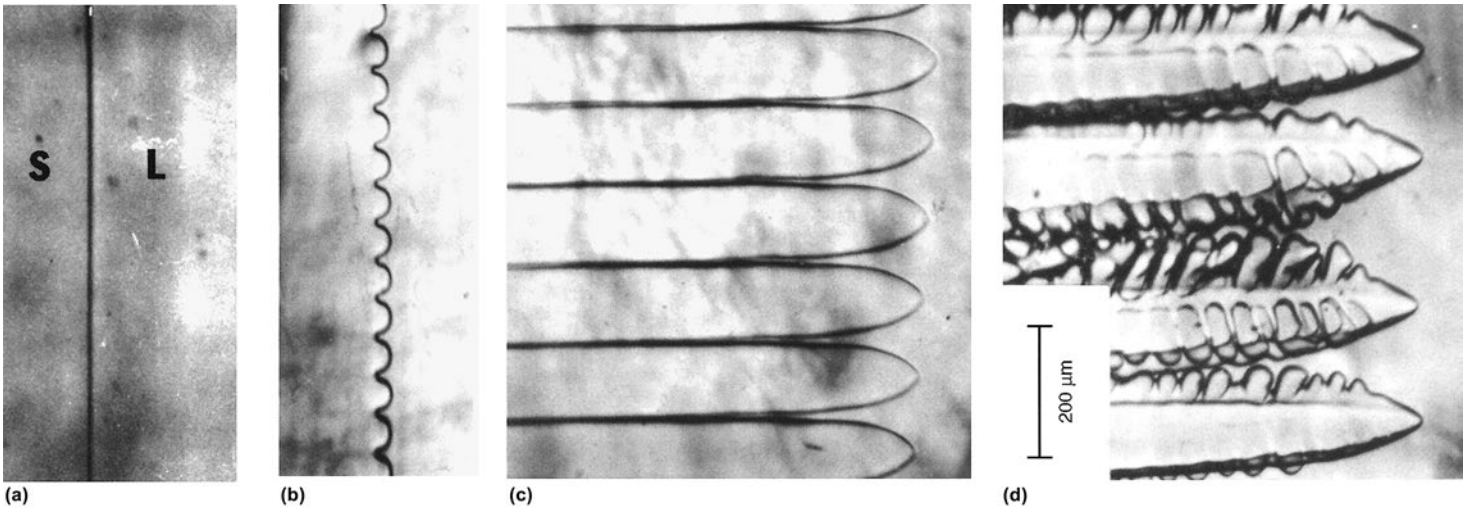

Fig. 13 Change of morphology of the solid/liquid (S/L) interface as a function of growth velocity (*V*) in a transparent organic system (pivalic acid, 0.076% ethanol) directionally solidified under a thermal gradient of 2.98 K/mm. (a) Planar interface, $V = 0.2$ µm/s. (b) Cellular interface, $V = 1.0$ µm/s. (c) Cellular interface, $V = 3.0$ µm/s. (d) Dendritic interface, $V = 7$ µm/s. Same scale for all images. Source: Ref 17

All the transitions described in the previous paragraph are controlled by the initial composition of the alloy, by the solidification velocity (V), and by the thermal gradient. The planar-to-cellular transition during steady-state solidification is governed by the criterion for the onset of constitutional undercooling given by:

$$\frac{G_T}{V} < -\frac{m_L C_o (1-k)}{k D_L} = \frac{\Delta T_o}{D_L} \qquad \text{(Eq 8)}$$

where k is the partition coefficient, D_L is the liquid diffusivity, and ΔT_o is the temperature difference between the equilibrium liquidus and solidus of the alloy of composition C_o. If solidification is not at steady state, ΔT_o is substituted with the undercooling ΔT at which solidification occurs.

Solidification Structures of Solid Solutions

The simplest liquid-to-solid transformation (solidification) of an alloy occurs when the liquid solution transforms into a solid solution (Fig. 15a). However, for many alloys, solidification may be completed by some other process, such as a eutectic (Fig. 15b), peritectic, or monotectic reaction. Because solidification of hypoeutectic cast iron starts with the solidification of austenite dendrites, which are solid solutions of carbon and other elements in iron, the details of the solidification of the solid solution are important in determining the final microstructure and thus the properties.

As shown in Fig. 8, the liquid has a different composition (C_L) than the solid (C_S) from which it is forming (in the figure, $C_L > C_S$). Consequences of this phenomenon are the occurrence of constitutional undercooling and segregation.

Constitutional undercooling is instrumental in destabilizing the S/L interface and promoting interface morphologies different than planar. As inferred by Eq 8, there is a critical solute content (C_o) of the alloy for a given G_T/V ratio combination, at which the interface becomes unstable. This can be presented graphically as shown in Fig. 16, where the line for Eq 8 indicates the planar-to-cellular transition. As the G_T/V ratio continues to decrease (or C_o to increase), the S/L interface becomes increasingly unstable with successive formation of a columnar dendritic and then equiaxed dendritic structure.

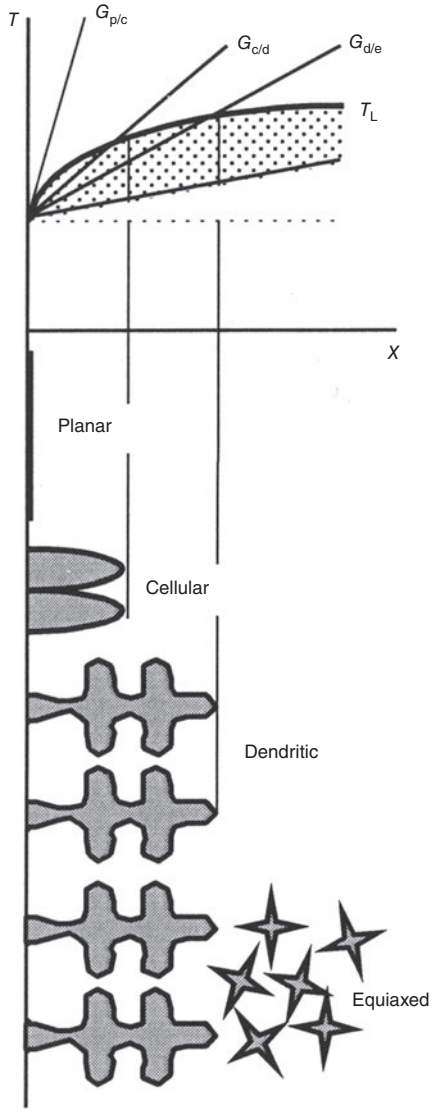

Fig. 14 Correlation between the thermal gradient at the interface and the interface morphology. Source: Ref 8

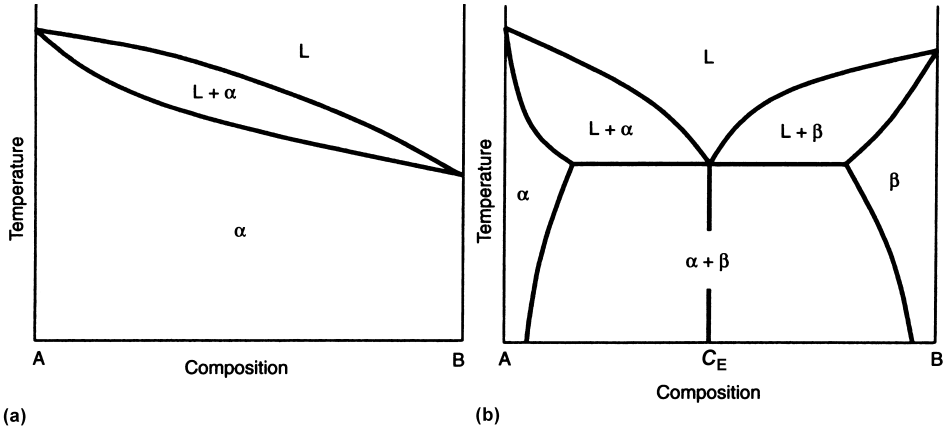

Fig. 15 Binary phase diagrams. (a) Complete solid solubility. (b) Partial solid solubility with eutectic reaction. L, liquid solution; α and β, solid solutions

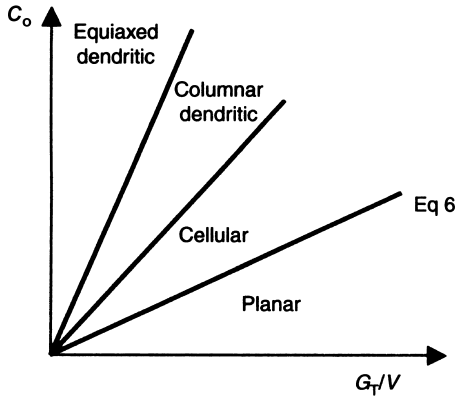

Fig. 16 Transition to different interface morphologies as a function of the temperature gradient/solidification velocity ratio (G_T/V) and solute concentration (C_o)

The formation of the equiaxed dendritic structure requires bulk nucleation. In the absence of bulk nucleation, the columnar front will continue to grow.

Planar Interfaces. Planar growth of alloys can usually be achieved only in crystal growth furnaces at high temperature gradients and low solidification velocities. For example, for planar solidification of an alloy with ΔT = 5 K and G_T = 100 K/cm, the maximum allowable solidification velocity calculated with Eq 8 is 2 μm/s. However, most commercial cast irons solidify with nonplanar interfaces, because the solidification velocity is much higher.

Cellular Structures. When constitutional undercooling occurs, the S/L interface morphology becomes cellular or dendritic. For conditions of growth where the G_T/V ratio is only slightly smaller than the ratio $\Delta T/D_L$, the interface is cellular, as shown in Fig. 17(a) for a hypoeutectic iron, after Tian and Stefanescu (Ref 20).

Dendritic Structures. The dendritic morphology is the most commonly observed solidification structure of solid solutions, including austenite in steel and cast iron. Examples of dendrites observed in directionally solidified cast iron are presented in Fig. 17(b, c).

Effect of Crystallographic Orientation. Dendrites are single grains that have preferred growth directions. The morphology of a columnar dendrite is influenced by the orientation of the grain with respect to that of heat extraction, as shown in Fig. 18, where the heat-extraction direction is upward (Ref 21).

Influence of the Type of Phase Diagram. The nature of the material as represented by the type of phase diagram will also influence the dendritic structures. If the phase diagram shows complete solid solubility (Fig. 15a), the structure will be single phase, containing only dendrites. If, as is the case for cast iron, the phase diagram contains a eutectic (Fig. 15b), the interdendritic regions will be composed of the two-phase eutectic. Figure 19, from Aguado et al. (Ref 22), presents a low-magnification microstructure of a hypoeutectic gray iron. The microstructure exhibits a large number of austenite dendrites with interdendritic austenite-graphite eutectic.

Effect of Constitutional Undercooling. As shown in Fig. 16, as the amount of solute increases, or as the G_T/V ratio decreases, a cellular-to-dendritic solidification occurs. This is because the constitutional undercooling is large. Such a transition is not common in cast iron, because the solidification conditions are conducive to mostly dendritic structures.

Figure 14 indicates that for rather steep thermal gradients, columnar dendrites will form, while for shallow gradients, equiaxed dendrite will solidify. In a continuously cooled casting, the decrease in the G_T/V ratio may produce a columnar-to-equiaxed transition, as seen in Fig. 4 for a gray iron bar.

Effect of Solidification Velocity. As emphasized previously, solidification velocity is, together with the temperature gradient, the most important variable affecting microstructure transitions. The change in solidification velocity may determine a planar S/L interface to become cellular and then dendritic. In addition, the morphology of the equiaxed dendrites (branching and tip radius) depends significantly on the cooling rate and/or undercooling. The effect of solidification velocity over a wide range of velocities can be understood from Fig. 20. At very small velocities, the dendrite tip radius is very large, even infinity, in which case a planar interface is obtained. As the velocity increases, the radius decreases, and the morphology changes from planar to globular/cellular, then to regular equiaxed dendritic. Further increase in solidification velocity in the range of rapid solidification determines a transition from fully branched to globular/cellular dendrites and finally again to planar interface (absolute stability). A typical example illustrating the influence of cooling rate on the morphology of equiaxed dendrites of an Al-7Si alloy is given in Fig. 21 (Ref 23).

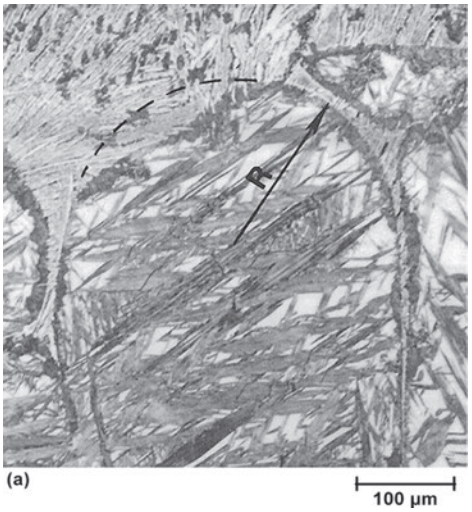

Fig. 17 Interface morphology at decanted solid/liquid interface in a Fe-3.08%C-2.01%Si alloy (G_T= 50 K/cm). (a) Austenite cell. (b) Array of austenite dendrites. (c) Paraboloid-shaped austenite dendrite tip. Source: Ref 20

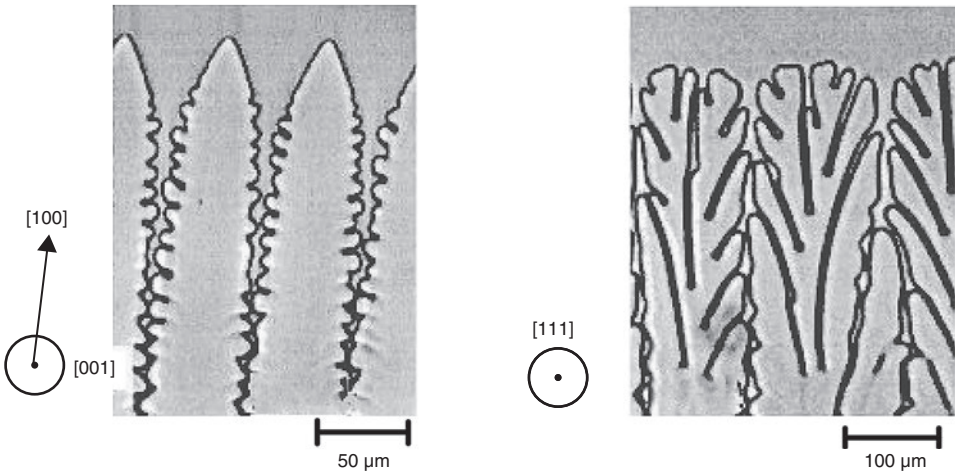

Fig. 18 Effect of crystalline anisotropy on interface shape in directional growth (growth velocity of 35 μm/s) of directional-solidification growth patterns in thin films of the CBr_4-8mol%C_2Cl_6 alloy. Source: Ref 21

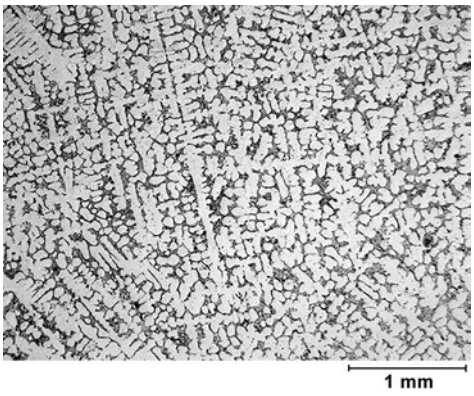

Fig. 19 Low-magnification micrograph of a hypoeutectic gray iron (3.26 carbon equivalent). Source: Ref 22

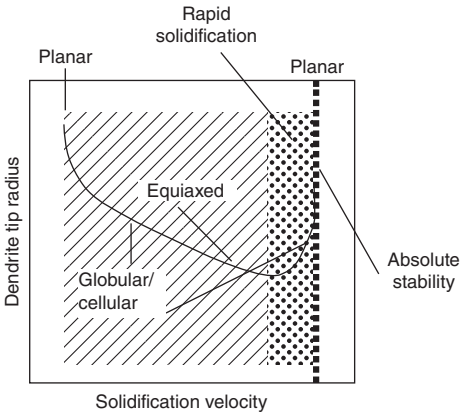

Fig. 20 Correlation between solidification velocity and dendrite tip radius. Source: Ref 8

The solidification time scale also influences the secondary dendrite arm spacing (SDAS). The SDAS is the distance between adjacent branches growing from the main dendritic arm. It is directly related to certain mechanical properties. It is generally accepted that the SDAS is a function of the local solidification time, t_f, described by:

$$\text{SDAS} = \mu_o \cdot t_f^{1/3} \quad \text{(Eq 9)}$$

where μ_o is a material-specific constant (coarsening constant). Extensive experimental data on secondary arm spacing have also been reported to fit a SDAS cooling-rate equation (Ref 24):

$$\text{SDAS} = \mu_1 \cdot (\dot{T})^{-0.34\pm0.02} \quad \text{(Eq 10)}$$

where μ_1 is a material-specific constant, and $\dot{T}$ is the cooling rate.

Solute Redistribution and Microsegregation in Dendritic Solidification. Rejection of solute from the solid during solidification that is responsible for the formation of the solutal boundary layer (Fig. 9) produces compositional nonuniformity across the dendrite during solidification, called microsegregation. To understand the mechanism of formation of microsegregation, consider the volume element extending from the axis of the dendrite arm to the edge of the final dendrite (at the end of solidification) shown in Fig. 22. The thick line in the lower part of the figure represents the composition change in the solid during solidification. At the beginning of solidification, when there is no solid formed, the fraction solid is $f_S = 0$. The first solid to form will have the composition $kC_o < C_o$. Assuming no diffusion in the solid and the liquid is of uniform composition, the amount of solute in the solid will continue to increase as solidification progresses. The composition of the solid will soon be higher than C_o; then it will reach the maximum solubility in solid, C_{SM}, and then the eutectic composition, C_E, according to the phase diagram in Fig. 8. The liquid still available will now solidify as eutectic. The composition of the solid (the thick line in Fig.) as well as the amount of eutectic at the end of solidification, f_E, can be calculated with the Gulliver-Scheil equation:

$$C_S = kC_o(1 - f_S)^{k-1} \quad \text{(Eq 11)}$$

Using this approach, it can be calculated that for a 3.5% C iron-carbon alloy, the first solid to form (the centers of dendrites) will have a composition of 1.75% C (at f_S= 0.01) and that the composition will increase to C_{SM} = 2.14% C when f_S = 0.335. The remaining fraction of the alloy (1 − 0.335 = 0.665) solidifies as an interdendritic

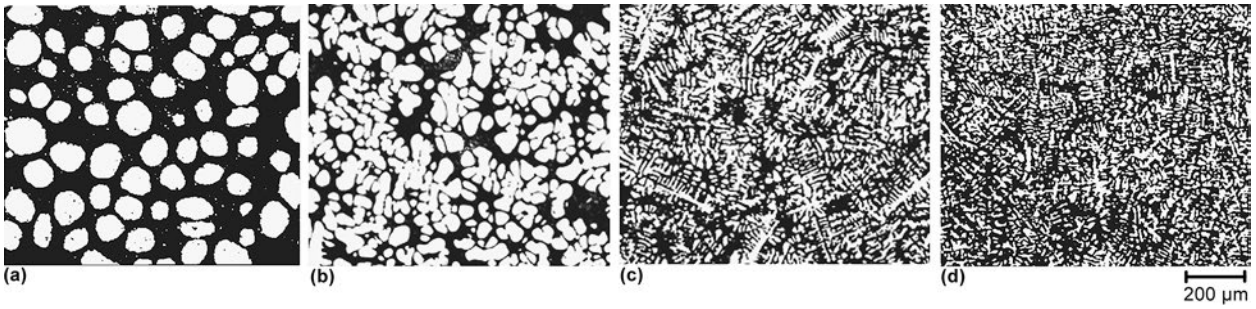

Fig. 21 Microstructures of an Al-7Si alloy at various cooling rates. (a) 0.3 °C/s (0.5 °F/s). (b) 3 °C/s (5 °F/s). (c) 10 °C/s (18 °F/s). (d) 30 °C/s (54 °F/s). Source: Ref 23

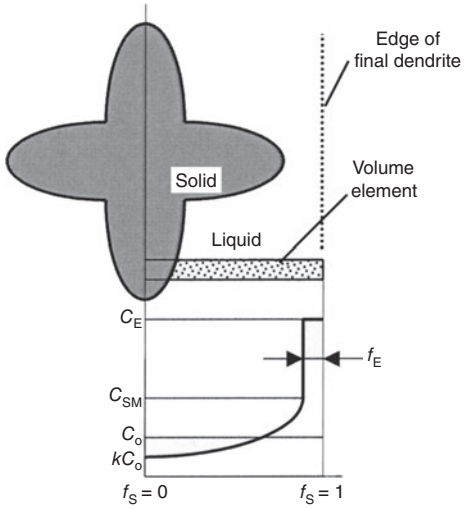

Fig. 22 Model of microsegregation occurring in the arm of a growing dendrite. C_E, eutectic composition; C_{SM}, maximum solubility in solid; f_S, solid fraction; f_E, amount of eutectic critical; C_o, initial composition of the alloy (bulk composition) at the beginning of solidification; k, partition coefficient; kC_o, composition of the first amount of solid to form

eutectic with an average composition of 4.3% C. The predictions of the Gulliver-Scheil equation should be used carefully. Generally, the equation tends to underestimate slightly the composition at the center of a dendrite and to overestimate the volume fraction of eutectic (for $k < 1$). Also, if extensive fluid flow exists through the dendritic or "mushy" zone, the average composition of the solidified castings may be significantly altered in regions that are large compared to the dendrite scale. This is called macrosegregation. Details regarding this subject and the field of solidification can be found in Ref 8.

Rapid Solidification. The microstructural length scale of solidified alloys generally decreases as the rate of heat extraction (cooling rate) increases. The term *rapid solidification* is normally applied to casting processes in which the liquid cooling rate exceeds 100 K/s (Ref 25). This definition is rather vague because different alloys respond very differently to high rates of cooling. Also, some microstructures observed in rapidly solidified alloys can be achieved by slow cooling when large liquid undercooling is achieved prior to nucleation (Ref 26).

Techniques usually used to produce rapidly solidified alloys are melt spinning, planar flow casting, or melt extraction, which produce thin (~25 to 100 μm) ribbon, tape, sheet, or fiber; atomization, which produces powder (~10 to 200 μm); and surface melting and resolidification, which produce thin surface layers. These methods may be considered casting techniques where at least one physical dimension of the final product is small. Consolidation is used to yield large products from rapidly solidified alloys (for example, through additive manufacturing techniques). This consolidation often alters the solidification microstructure in final products. However, as with ordinary castings, many features of the solidification structure can remain in the final product (Ref 25).

The effect of high cooling rates on the dendrite morphology can be understood from Fig. 20. It is seen that as the cooling rate increases in the rapid-solidification range, the tip radius increases. This also means that branching decreases and the equiaxed dendrite will become globular/cellular. However, these types of structures are not found in commercial cast iron, because high cooling rates will be conducive to metastable solidification and thus carbide structures.

Solidification Structures of Eutectics

Eutectics are alloys that have a fixed composition in terms of species A and B and solidify as two-phase solids ($\alpha + \beta$). The phase diagram in Fig. 15(b) shows a binary eutectic invariant point at temperature T_E and composition C_E. At this point, two solid phases, α and β, solidify simultaneously from the liquid, L. The eutectic reaction can be written as: $L \rightarrow \alpha + \beta$. As many as four phases have been observed to grow simultaneously from the melt. However, most technologically useful eutectic alloys consist of two phases. The particular morphology of the eutectic is a function of processing conditions and of the nature of the two phases.

Classification of Eutectics. Many eutectic classifications have been proposed, based on different criteria. A first classification of eutectics based on their growth mechanism is:

- *Cooperative growth:* The two phases of the eutectic grow together as a diffusion couple.
- *Divorced growth:* The two phases of the eutectic grow separately; there is no direct exchange of solute between the two solid phases and no trijunction.

Cooperative eutectics can be further classified based on the ratio between the fractions of the two phases of the eutectic, f_α and f_β, and on the morphology of the S/L interface (Ref 27), as shown in Fig. 23. The nondimensional entropy of fusion, $\Delta S_f/R$, where R is the gas constant, is used to distinguish between faceted and nonfaceted morphologies.

Alloys such as lead-tin and Al-Al_2Cu, where there are approximately equal volume fractions of nonfaceted phases, solidify as regular, lamellar eutectics. If one of the phases is nonfaceted, the morphology becomes irregular, because the faceted phase grows preferentially in a direction determined by specific atomic planes. This is the case of lamellar graphite iron, where austenite is nonfaceted and graphite is faceted. In this case, one solid phase may project into the liquid far in advance of the other solid phase.

When the volume fraction of one phase is significantly lower than that of the other (typically < 0.28), a fibrous structure will result (for example, the Ni-NbC eutectic). This is a result of the tendency of the system to minimize its interfacial energy by selecting the morphology that is associated with the smallest interfacial area. Fibers have smaller interfacial area than lamellae. However, when the minor phase is faceted, a lamellar structure may form even at a very low volume fraction, because specific planes may have the lowest interfacial energy. The minor phase will then grow such as to expose these planes even when lamellae rather than fibers are formed. The two commercially most significant eutectics, aluminum-silicon and iron-graphite, fall into this category. Note that in the iron-graphite eutectic, the fraction graphite is $f_{Gr} = 0.07$. The iron-graphite eutectic can be either cooperative, irregular, as

is the case of lamellar graphite cast iron, or divorced, as for spheroidal graphite cast iron. In this last case, at the beginning of solidification the two phases, graphite and austenite dendrites, grow independently from the liquid without establishing a diffusion couple.

Operating Compositional Range. From the eutectic phase diagram, it appears that a eutectic structure can be obtained only when the composition is exactly eutectic. Nevertheless, both experiments and theory show that, depending on the growth conditions, eutectic microstructures can be obtained at off-eutectic compositions. Such conditions include a sufficiently steep gradient or slow solidification velocity during directional solidification. This is possible because the eutectic grows faster than the dendrites, because diffusion-coupled growth is much faster than isolated dendritic growth. Accordingly, even in off-eutectic compositions, the eutectic may outgrow the individual dendrites, resulting in a purely eutectic microstructure. On the other hand, at high growth velocities, dendrites can be found in alloys of eutectic compositions.

An analysis of the possible solidification microstructure of a binary alloy can be made based on the growth velocities of the competing phases. On the phase diagram in Fig. 24(a), the three shaded regions extending under the eutectic invariant form a coupled zone. This is a solidification-velocity-dependent composition region in which the eutectic grows more rapidly, or at a lower undercooling, than the α or β dendrites. For regular eutectics, the coupled zone is symmetric. Note that the widening of the coupled zone near the eutectic temperature is observed only in directional solidification, where the thermal gradient is positive.

For small undercooling, the S/L interface is planar. As shown on the right side of Fig. 24(a), even for a hypereutectic alloy solidifying at small undercooling, the eutectic has the highest growth velocity, and a planar, coupled eutectic is produced. At higher undercooling, the β phase will have higher growth velocity, and a eutectic-dendritic structure will result. At even higher undercooling, the eutectic velocity will again become the highest. However, because of the undercooling, a planar structure is not possible, and equiaxed coupled growth will result.

If one of the eutectic phases is faceted, the growth of this phase and consequently that of the eutectic is slowed down. Dendrites of the other phase may grow faster at a given undercooling than the eutectic, even for the eutectic composition. Consequently, purely eutectic microstructures can be obtained only at hypereutectic compositions. This is exemplified in Fig. 24(b) for the case of faceted β phase. An asymmetric coupled zone results.

From Fig. 24(a) it can be noted that as the undercooling increases, the microstructure of the eutectic changes from planar to cellular, dendritic, and then equiaxed. When the alloy

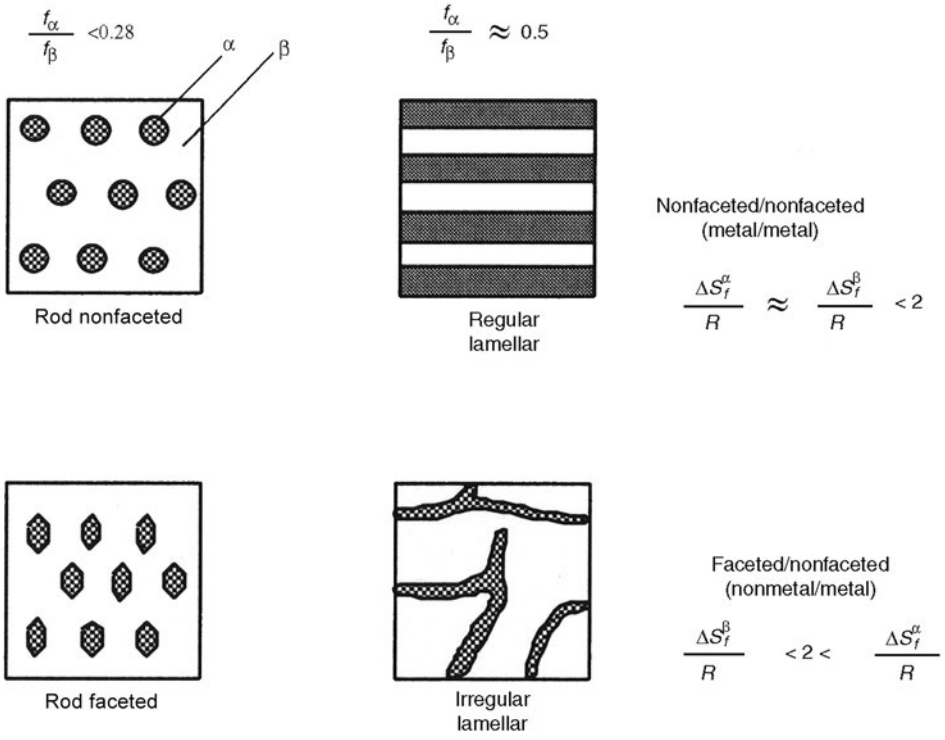

Fig. 23 Types of cooperative eutectics. Source: Ref 27

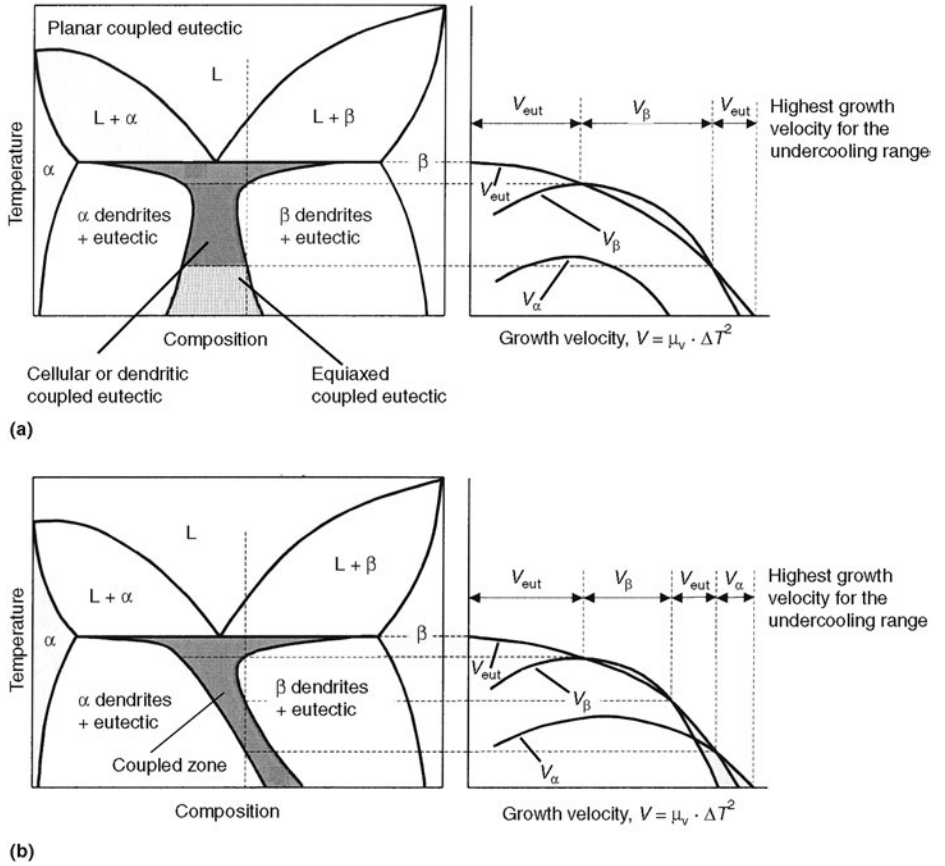

Fig. 24 Coupled eutectic zones. (a) Symmetric coupled zone (regular eutectics). (b) Asymmetric coupled zone (irregular eutectics). Source: Ref 8

solidifies with a cellular rather than a planar interface, eutectic colonies are formed.

If the undercooling is high, equiaxed eutectic grains may form even during directional solidification. A typical example is given in Fig. 12 (c) for a gray cast iron. The boundaries of the grains are outlined because of the segregation of phosphorus and the formation of a low-melting-point phosphide eutectic.

Caution must be exercised during metallographic analysis of eutectic microstructures. Serial sectioning, phase-extraction techniques, and examination of two sections meeting at a common edge have revealed that the microstructures of most eutectics cannot be considered aggregates of many simply-shaped, discrete particles of one phase embedded in a matrix of the other phase or phases. Rather, if the three-dimensional shapes of all phases are examined, the apparently individual particles of each phase are typically found interconnected in a topologically complex arrangement. This is the case for compacted graphite iron.

Length Scale of Eutectics. The length scale of the eutectic strongly affects the mechanical and physical properties of the eutectic aggregate. For cooperative eutectics, the length scale is given by the lamellar spacing (interlamellar or interfiber) spacing, which is affected by solidification velocity, thermal gradients, undercooling, atomic bonding, relative amounts, crystallographic factors, interfacial energies, impurity content, and alloy composition. The lamellar spacing, λ, and the solidification velocity are related by the simple equation $\lambda^2 V$ = constant. The effect of solidification velocity is illustrated in Fig. 25. It is seen that the spacing of irregular eutectics is significantly larger than that of regular eutectics.

The adjustment in the eutectic spacing during growth occurs through faults. Two types of faults are shown in Fig. 26. Figure 26(a) shows a no-net fault in which the number of lamellae on both sides of the fault is the same. Figure 26(b) shows a net fault in which one side of the fault has one more lamellae than the other side. This fault is analogous to an extended dislocation in that the number of lamellae above and below the fault differ by one (Ref 28).

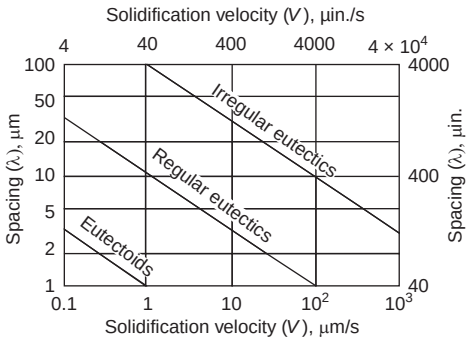

Fig. 25 Comparison of the lamellar spacing/solidification velocity correlation for eutectics and eutectoids. Source: Ref 8

For equiaxed eutectics, the length scale may include grain size in addition to lamellar spacing. Metallographic identification of the grain size is alloy specific.

Solidification Structures of Peritectics

Peritectic solidification is very common in the solidification of metallic alloys. Many technically important alloy systems, such as steels, copper alloys, and rare-earth permanent magnets, display peritectic reactions in the regions of their phase diagrams where phase and microstructure selection play an important role for the processing and the properties of the material. Basically, peritectic solidification means that at the peritectic temperature, T_P, a solid phase γ of peritectic composition, C_P, solidifies from a mixture of liquid, L, and solid phase δ. The peritectic solidification can be written as $L + \delta \rightarrow \gamma$. A phase diagram with peritectic solidification is presented in Fig. 27. The different reactions occurring along the solidus lines, corresponding to various compositions, produce three structural regions: $\delta + \gamma$, γ, and $L + \gamma$.

Two different mechanisms are involved in peritectic solidification: peritectic reaction and peritectic transformation. These mechanisms are shown in Fig. 28. In a peritectic reaction, all three phases (δ, γ, and liquid) are in contact with each other. In the peritectic transformation, the liquid and the primary δ phase are isolated by the γ phase. The transformation takes place by long-range diffusion through the secondary γ phase. A variety of microstructures can result from peritectic solidification, mostly depending on the G_T/V ratio and nucleation conditions. The possible structures include cellular, plane-front, bands, and eutectic-like structures.

Simultaneous growth of two phases in the form of oriented fibers and lamellae has been

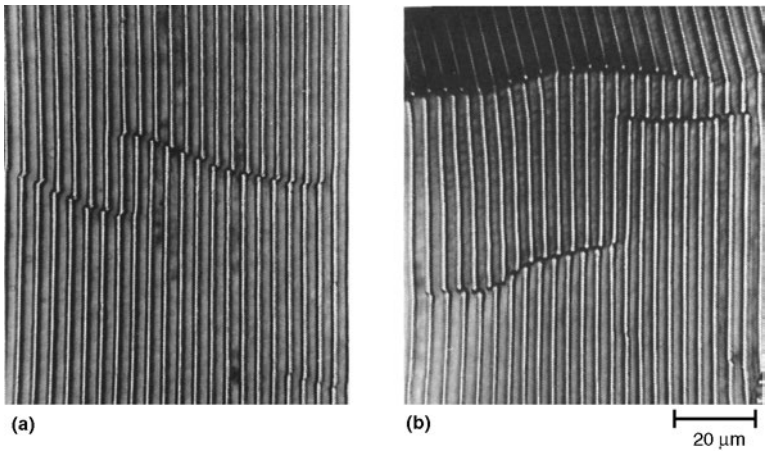

Fig. 26 Cross sections of a directionally solidified lead-cadmium eutectic showing the presence of faults in the lamellae. (a) No-net fault. (b) Net fault. Etchant not reported. Source: Ref 28

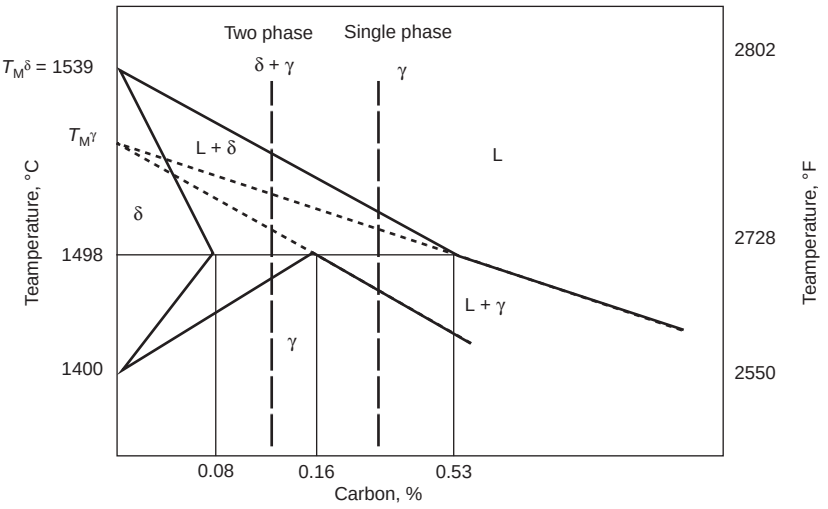

Fig. 27 Schematic phase diagram of the peritectic region of carbon steel. Source: Ref 8

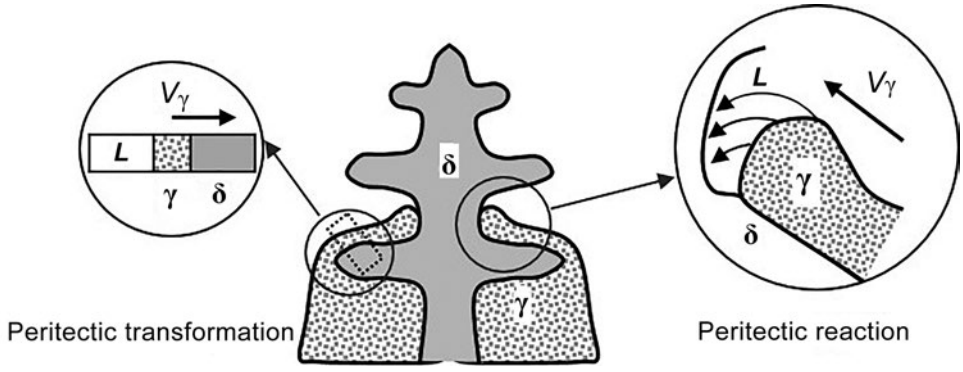

Fig. 28 Mechanisms of peritectic solidification. Source: Ref 8

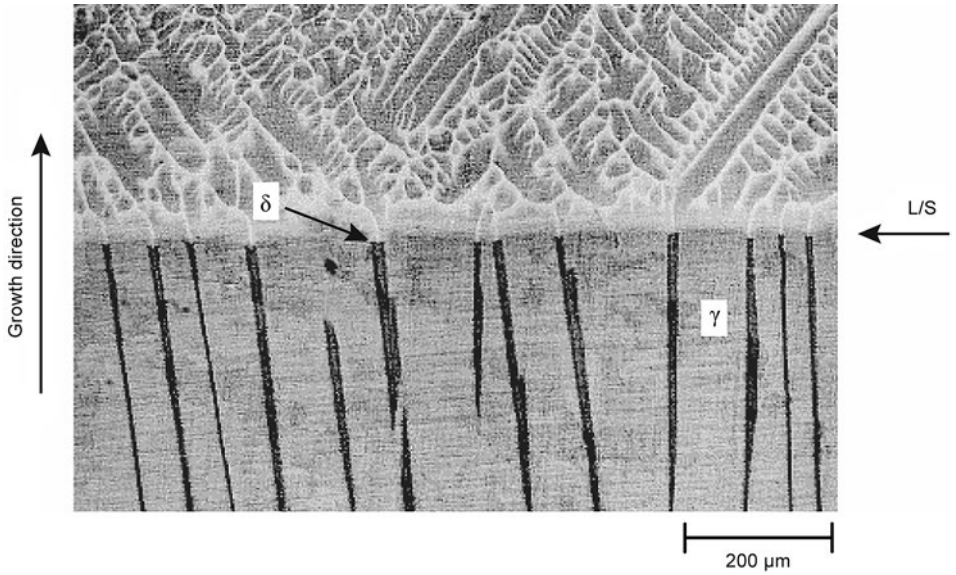

Fig. 29 Quenched solid/liquid interface of simultaneous two-phase growth in peritectic iron-nickel alloy. Source: Ref 29

observed in some peritectic alloys when the composition was on the tie-line of the two solid phases and the G_T/V ratio was close to the limit of constitutional undercooling for the stable phase having the smaller distribution coefficient (Ref 29). Figure 29 shows such a structure for an iron-nickel alloy.

Fluid flow can further complicate the possible microstructures. While peritectic reactions are typical for cast steel, they do not occur in cast iron, because the carbon content is always above the higher limit (0.53%) of the peritectic solidus.

ACKNOWLEDGMENT

This article was adapted from Doru M. Stefanescu and Roxana Ruxanda, Fundamentals of Solidification, *Metallography and Microstructures*, Volume 9, *ASM Handbook*, American Society for Metals, 1985, p 71–92.

REFERENCES

1. M.V. Volostchenko, On the State of Graphite in Liquid Iron, *Liteinoe Proizvod*., No. 2, 1976, p 5–7
2. S. Steeb and U. Maier, in *The Metallurgy of Cast Iron*, B. Lux, I. Minkoff, and F. Mollard, Ed., Georgi Publishing, St. Saphorin, Switzerland, 1974, p 1–11
3. W. Krieger and H. Trenkler, *Arch. Eisenhüttenwes*., Vol 42 (No. 3), 1971, p 175
4. L.S. Darken, "Equilibria in Liquid Iron with Carbon and Silicon," Tech. Pub. 1163, AIME Metals Technology, 1940, p 1
5. E. Schürmann, private communication quoted in Ref 1
6. A.A. Vertman and A.M. Samarin, *Dokl. Akad. Nauk SSSR*, Vol 134 (No. 3), 1960, p 629
7. A.A. Vertman and A.M. Samarin, *Liteinoe Proizvod*., No. 10, 1964
8. D.M. Stefanescu, *Science and Engineering of Casting Solidification*, 3rd ed., Springer, 2015
9. R.E. Boeri and J.A. Sikora, *Int. J. Cast Met. Res*., Vol 13 (No. 5), 2001, p 307–313
10. J.C. Moore, in *Metallography, Structures and Phase Diagrams*, Vol 8, *Metals Handbook*, 8th ed., American Society for Metals, Metals Park, OH, 1973, p 93
11. G.R. Purdy and M. Audier, Electron Microscopical Observations of Graphite in Cast Irons, *The Physical Metallurgy of Cast Iron*, H. Fredriksson and M. Hillert, Ed., Materials Research Society Symposia Proc. (Stockholm), North-Holland, New York, 1985, p 13–23
12. D.M. Stefanescu, G. Alonso, P. Larrañaga, and R. Suarez, On the Stable Eutectic Solidification of Iron-Carbon-Silicon Alloys, *Acta Mater*., Vol 103, 2016, p 103–114
13. D. Turnbull and R. Vonnegut, *Ind. Eng. Chem*., Vol 44, 1952, p 1292
14. B. Bramfitt, *Metall. Trans*., Vol 1, 1970, p 1987–1995
15. A.L. Greer, A.M. Bunn, A. Tronche, P.V. Evans, and D.J. Bristow, *Acta Mater*., Vol 48, 2000, p 2823
16. R. Elliott, *Cast Iron Technology*, Butterworths, London, 1988
17. R. Trivedi and W. Kurz, Solidification of Single-Phase Alloys, *Casting*, Vol 15, *ASM Handbook*, D.M. Stefanescu, Ed., ASM International, 1988, p 114
18. H. Tian, Ph.D. dissertation, University of Alabama, Tuscaloosa, 1992
19. H. Tian and D.M. Stefanescu, Experimental Evaluation of Some Solidification Kinetics-Related Material Parameters Required in Modeling of Solidification of Fe-C-Si Alloys, *Modeling of Casting, Welding and Advanced Solidification Processes-VI*, T.S. Piwonka, V. Voller, and L. Katgerman, Ed., TMS, Warrendale, PA, 1993, p 639
20. H. Tian and D.M. Stefanescu, Dendritic Growth during Directional Solidification of Hypoeutectic Fe-C-Si Alloys, *Metall. Trans. A*, Vol 23, 1992, p 681–687
21. S. Akamatsu, G. Faivre, and T. Ihle, *Phys. Rev. E*, Vol 51, 1995, p 4751–4773
22. E. Aguado, D.M. Stefanescu, J. Sertucha, P. Larrañaga, and R. Suárez, Effect of Carbon Equivalent and Alloying Elements on the Tensile Properties of Superfine Interdendritic Graphite Irons, *Trans. AFS*, Vol 122, 2014, p 249–258
23. C.P. Hong and M.F. Zhu, in *The Science of Casting and Solidification*, D.M. Stefanescu,

R. Ruxanda, M. Tierean, and C. Serban, Ed., Editura Lux Libris, Brasov, Romania, 2001, p 110–118
24. D. Bouchard and J.S. Kirkaldy, *Metall. Mater. Trans. B*, Vol 28, 1997, p 651
25. W.J. Boettinger, *Metall. Mater. Trans.*, Vol 5, 1974, p 2026
26. J.H. Perepezko and J.J. Paike, in *Rapidly Solidified Amorphous and Crystalline Alloys*, B.H. Kear, B.C. Giessen, and M. Cohen, Ed., North-Holland, 1982, p 49
27. W. Kurz and D.J. Fisher, *Fundamentals of Solidification*, 3rd ed., Trans Tech Publications, Switzerland, 1989
28. R. Trivedi, J.T. Mason, J.D. Verhoeven, and W. Kurz, *Metall. Mater. Trans. A*, Vol 22, 1991, p 2523–2533
29. M. Vandyoussefi, H.W. Kerr, and W. Kurz, *Acta Mater.*, Vol 48, 2000, p 2297–2306